AIMS Materials Science, 8(3): 359–372.
DOI: 10.3934/matersci.2021023
Received: 23 February 2021
Accepted: 13 May 2021
Published: 26 May 2021

http://www.aimspress.com/journal/Materials

Research article

Williamson–Hall based X-ray peak profile evaluation and nano-structural characterization of rod-shaped hydroxyapatite powder for potential dental restorative procedures

Supriya Rattan, Derek Fawcett, and Gerrard Eddy Jai Poinern*

Murdoch Applied Nanotechnology Research Group. Department of Physics, Energy Studies and Nanotechnology, Murdoch University, Murdoch, Western Australia 6150, Australia

* **Correspondence:** Email: G.Poinern@murdoch.edu.au.

Abstract: In the present paper, nanometer scale hydroxyapatite powders with a rod-like shape, were prepared using a combined ultrasonic and microwave heating-based method. Subsequent annealing of as-synthesized powders at 800 °C for 2 h produced nanoparticles with a rectangular and granular morphology. The hydroxyapatite particles were characterized using X-ray diffraction and Fourier transform infrared spectroscopy methods. Also, nanoparticle size and morphology were investigated using transmission electron microscopy and field emission scanning electron microscopy. A comparable selected area electron diffraction (SAED) analysis also showed results in line with X-ray powder diffraction patterns. The resulting X-ray diffraction peaks indicated that the powders were highly crystalline in nature and no impure phases were present. The X-ray diffraction data, was also used to study the effects of peak broadening by using the Williamson–Hall (W–H) analysis technique. The analysis used the uniform deformation model (UDM), uniform stress deformation model (USDM) and uniform deformation energy density model (UDEDM) to determine physical parameters like crystallite size, lattice strain, stress and energy density. The results of the W-H analysis were found to be comparable to the results obtained from microscopy studies. Importantly, the studies confirmed the synthesized nano- hydroxyapatite powders had morphologies similar to those found in dental hard tissues.

Keywords: hydroxyapatite; ultrasonic synthesis; biomedical; X-ray peak analysis

1. Introduction

There is an increasing numbers of dental reports in the literature reporting the prevalence of periodontal diseases affecting a large portion of the global population. Human teeth are composed of three different types of calcified tissues, which categorizes teeth as hard tissue. These calcified tissues consist of enamel, dentine and cementum. The upper region of a tooth (above the gum) is the enamel-coated crown and directly experiences the tearing and grinding of food during mastication. The thin enamel coating (<1 mm) is brittle and the hardest material present in the human body. It is composed of calcium-deficient carbonate hydroxyl apatite (96 wt%), with the balance of the weight made up by organic materials and water [1]. While the underlying dentine, which is not as hard as enamel, is composed of a three dimensional organic scaffold structure reinforced by numerous embedded hydroxyapatite crystallites (~20 nm) [2].

Naturally occurring hydroxyapatite (HAP) is a mineral composed of calcium phosphate groups that form a hexagonal lattice structure. The unit cell is expressed by the general formula of $[Ca_{10}(OH)_2(PO_4)_6]$. Chemical and crystallographic studies have shown the close physiochemical similarity between synthetic HAP and natural HAP found in both enamel and dentine [3,4]. The results of several studies have shown there are four advantages of using synthetic HAP in dental and medical procedures. These advantages include: (1) good biocompatibility with surrounding tissues; (2) slow biodegradability in situ; (3) good osteoconductivity, and (4) good osteoinductivity [5,6]. Interestingly, HAP-based pastes are currently used in dental procedures to treat surface discolorations, chips and voids in enamel, and as re-mineralizing agents in toothpastes [7,8]. While granular forms of HAP are currently used in dental procedures like: (1) restoration of periodontal bone defects [9]; (2) edentulous ridge augmentation [10]; (3) increasing the thickness of atrophic alveolar ridges; (4) filling bone defects after cystectomy; (5) endodontic treatment procedures such as repairing bifurcation perforations and pulp-capping [11,12] and (6) dental implant coating [13]. Because of the close chemical similarity between synthetic HAP and natural HAP, research has focused on developing new methods for synthesizing synthetic HAP with specific physiochemical properties suitable for use in preventative and restorative dental procedures. In recent years nanotechnology-based techniques have been able to synthesize functionalized nanomaterials with tailored and enhanced properties. Thus, making the properties of these new nanomaterials superior to the properties of their bulk equivalents [14,15].

In this article, we discuss the properties of a synthetic nanometer scale hydroxyapatite (nano-HAP) powder that was synthesized using a combined ultrasonic and microwave assisted method as a potential restorative material for dental procedures. X-ray peak analysis plays an important role in estimating the microstructural quantities such as crystallite size and lattice strain and correlate them to the observed material properties. Crystallite size and lattice strain both affect the Bragg peak in different ways, for instance, crystallite size varies as $1/\cos\theta$ while the strain varies as $\tan\theta$ from the peak width [16]. The Williamson–Hall based X-ray peak analysis technique was used to determine powder properties like crystallite size ($D_{(hkl)}$), lattice strain (ε), stress (σ) and energy density (u). The analysis utilized the uniform deformation model (UDM), uniform stress deformation model (USDM) and uniform deformation energy-density model (UDEDM) to generate an idea about stress-strain relation and strain as a function of energy density (u). A comparative evaluation of the particle size of nano-hydroxyapatite rods obtained from TEM, SEM, SAED measurements and from powder X-ray diffraction peak broadening is also reported in present

research. Furthermore, Fourier transform infrared spectroscopy (FT-IR) was used to identify functional groups, their respective vibration modes and possible impurities in the samples. Elemental analysis of the samples was investigated using energy dispersive spectroscopy (EDS). While transmission electron microscopy (TEM) and field emission scanning electron microscopy (FESEM) were used to determine the overall size and shape of the respective samples.

2. Materials and methods

2.1. Materials

All chemicals used in this study were procured from Chem. Supply (Australia) and Sigma Aldrich (USA). The aqueous reagents were prepared using Milli-Q® water (18.3 $M{\cdot}\Omega{\cdot}cm^{-1}$) produced by an ultrapure water system (Barnstead Ultrapure Water System D11931; Thermo Scientific, Dubuque, IA). Chemical synthesis was carried out using a Hielscher Ultrasound Processor UP400s operating at maximum power of 400 W and 24 kHz.

2.2. Methods

2.2.1. Preparation of nanometer scale hydroxyapatite powders

Formulation of nano-HAP began by decanting a 40 mL solution of 0.32 M $Ca(NO_3)_2{\cdot}4H_2O$ into a small beaker and then kept under ultrasonic irradiation. The ultrasound processor used was a UP400S supplied by Hielscher Ultrasound Technology (Teltow, Germany). The processor was fitted with a 22 mm diameter sonotrode operating at 24 kHz and set to maximum amplitude and operating power of 200 W. During the ultrasonic processing (1 h), the solution pH was maintained above 9 using a 5 mL of NH_4OH solution that was added at regular intervals. Then a 60 mL solution of 0.19 M [KH_2PO_4] was slowly added drop-wise to the above solution under ultrasonic irradiation conditions. The mixture was then subjected to ultrasonic processing for a further 20 min. The solution pH was kept above 9 and the Ca/P ratio of 1.67 was maintained throughout the process. After processing, the mixture underwent centrifugation at 3500 rpm for 20 min to separate the white precipitate that had formed during processing from the mixture. Following centrifugation, the white precipitate underwent washing with Milli-Q® water several times. The precipitate was then heated in a 240 V and 50 Hz microwave oven (Model TMOSS25) operating at 900 W and 2450 MHz for a 12-minute treatment period. After treatment, samples were ground to the consistency of an ultrafine powder using mortar and pestle. After powder grinding, a selection of powders were annealed at 800 °C for 2 h. All powders were then studied using advanced characterization techniques.

2.2.2. X-ray powder diffraction studies

X-ray Diffraction (XRD) spectroscopy was carried out on all powder samples using a GBC® eMMA X-ray Powder Diffractometer (CuKα = 1.54056 Å radiation source) operating at 35 kV and 28 mA. Diffraction patterns were recorded over a 2θ range starting at 10° and finishing at 80°. The incremental step size used over the 2θ range was 0.04° and the acquisition speed was $1°{\cdot}min^{-1}$. From the resulting XRD patterns, the Bragg peak positions were identified and compared to those

reported in the ICDD (International Centre for Diffraction Data) databases and were assigned the appropriate Miller indices. Peak broadening data from the XRD patterns were studied using the Williamson–Hall (W–H) analysis technique to determine physical parameters like crystallite size, strain, stress and energy density.

2.2.3. Fourier transform infrared spectroscopy (FT-IR)

Fourier transform infrared spectroscopy (FT-IR) was used to identify functional groups and their respective vibration modes present in the samples using a PerkinElmer FT-IR/NIR Spectrometer Frontier fitted with a universal signal bounce Diamond ATR attachment. The dry samples were thoroughly mixed and placed onto the FTIR top-plate sample holder using the pressure arm accessories. FT-IR spectra were recorded over the wavenumber interval of 400 to 4000 cm^{-1} with a resolution step of 1 cm^{-1}.

2.2.4. Electron Microscope and Energy Dispersive Spectroscopy

Initial particle size and shape were obtained from a JEOL JCM-6000, NeoScope^{TM} electron microscope. Prior to imaging, samples were dried, fitted to holders using copper adhesive tape and sputter coated using an E5000 sputter coater (Polaron Equipment Ltd). The deposited coating consisted of a 2 nm layer of platinum to prevent charge build up. While the energy dispersive spectroscopy (EDS) attachment of the NeoScope^{TM} electron microscope was used for the elemental analysis of each sample. High resolution sample images were taken using a field emission scanning electron microscope (FESEM: FEI-Verios 460 XHR) operating at 5 kV, with 0.10 nA current and operating under secondary electron mode. The immersion lens in the FESEM column and FEI imaging software were used for generating nanometer scale images. Morphological analysis of the samples were done using an FEI-TITAN G2 80-200 Transmission Electron microscope (TEM) operated at 200 kV bright-field mode (installed at Centre for Microscopy, Characterization and analysis, University of Western Australia).

3. Results and discussions

3.1. XRD and Williamson–Hall based X-ray peak analysis

Representative XRD patterns for as-synthesized stoichiometric nano-HAP powder and a subsequently annealed sample are presented in Figure 1. Both samples clearly display several diffraction peaks that indicate a polycrystalline structure. The observed peak positions in the respective patterns were indexed and compared to those reported by the Joint Committee on Powder Diffraction Standard (JCPDS No. 09-0432) for pure hexagonal crystalline hydroxyapatite.

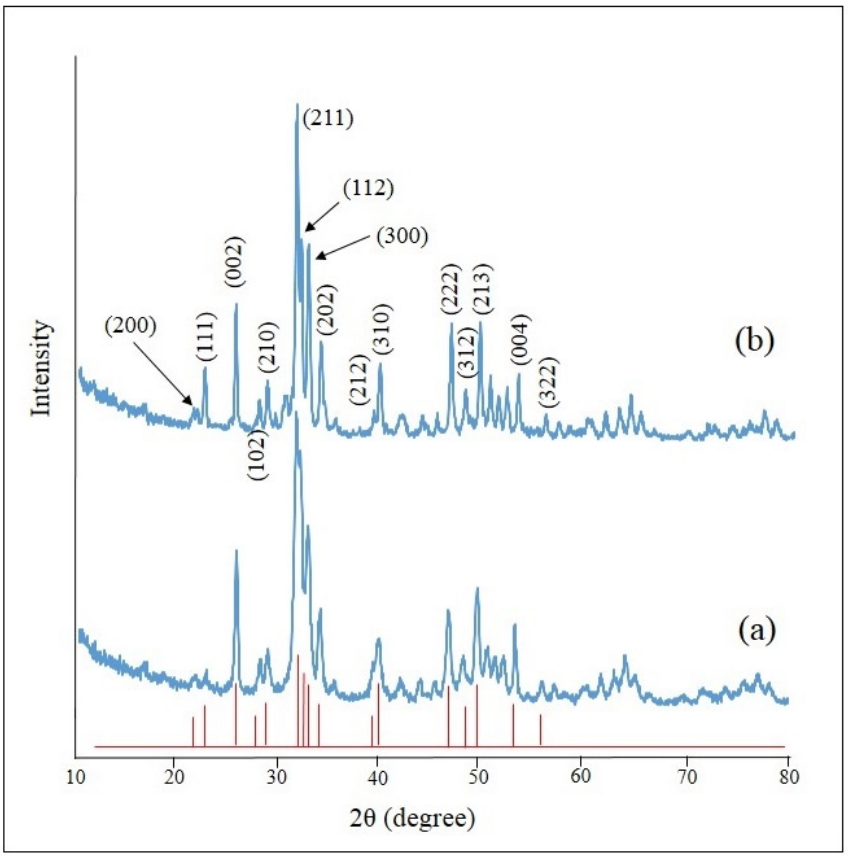

Figure 1. XRD patterns of nano-HAP: (a) as synthesized and (b) after annealing at 800 °C for 2 h.

In each case the appropriate Miller indices were assigned to the respective peaks as seen in Figure 1. Also seen in Figure 1 are changes in intensity and sharpness of the peaks in the annealed pattern compared to the as-synthesized sample. This clearly indicates improved crystallinity and increased crystallite size in the annealed sample. This feature has also been seen in similar studies reported in the literature [15,17]. The crystallinity of the samples was also confirmed by the ring patterns generated by selected area electron diffraction (SAED). A representative SAED pattern is presented in Figure 2a. Importantly, the presence of impurities, if any, were well below the detection limit of X-ray diffractometer and subsequent analysis. Crystallite sizes were calculated using both the Scherrer ($DS_{(hkl)}$) Eq 1 and the Williamson–Hall ($D_{(hkl)}$) Eq 2. In addition, the Williamson–Hall analysis technique was also used to determine strain (ε), stress (σ) and anisotropic energy density (u).

$$D_{s\,(hkl)} = \frac{k\lambda}{\beta_{(hkl)}\ \cos\theta_{(hkl)}} \tag{1}$$

$$\beta_{(hkl)}\ \cos\theta = \frac{k\lambda}{D_{(hkl)}} + 4\varepsilon \sin\theta \tag{2}$$

where λ is the wavelength of the monochromatic X-ray beam and k is the crystallite shape constant k,

which is 0.9 for spherical crystals with cubic unit cells. And β is the Full Width at Half Maximum (FWHM) of the peak at the maximum intensity, $\theta_{(hkl)}$ is the peak diffraction angle that satisfies Bragg's law for the (*hkl*) plane, ε is the strain, and $Ds_{(hkl)}$ and $D_{(hkl)}$ are the respective crystallite sizes.

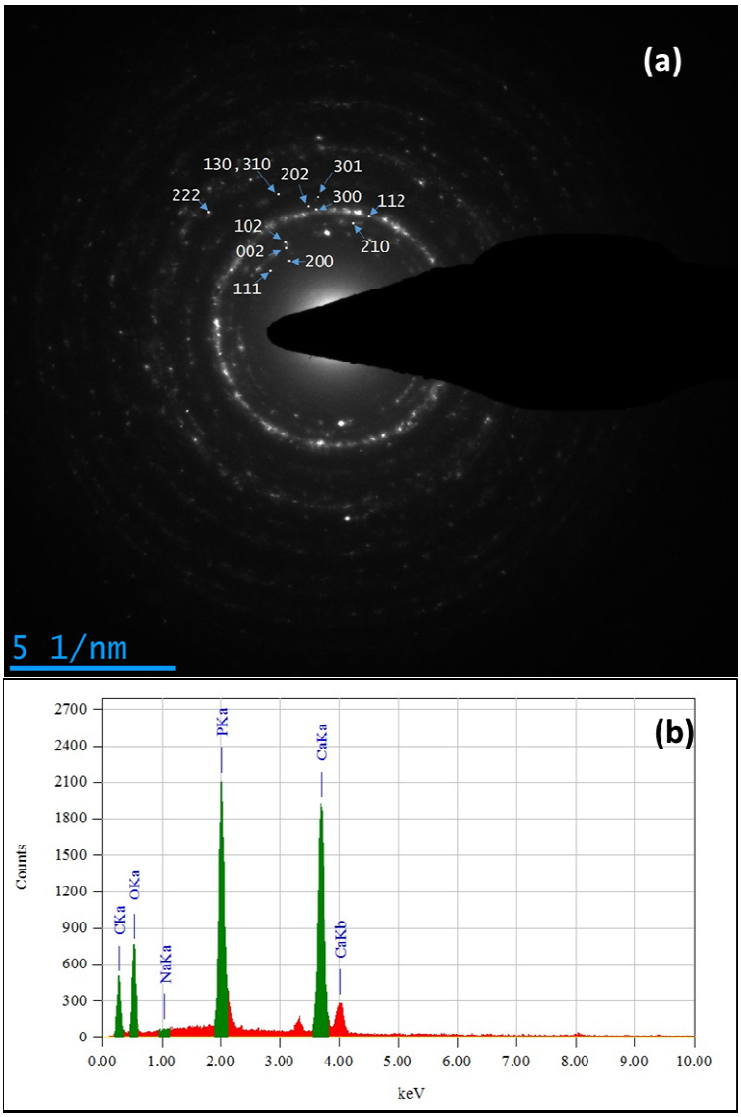

Figure 2. (a) SAED pattern of the as-synthesized hydroxyapatite crystals; (b) representative EDS elemental analysis.

Equation 2 represents the uniform deformation model (UDM) and assumes strain is uniform in all crystallographic directions and material properties are independent of the direction along which measurements are made. Thus, plotting $4sin\theta$ along the x-axis and $\beta_{(hkl)}cos\theta$ along the y-axis enables a linear fit to the data. From the plot both slope (ε) and (y-intercept) crystallite size ($D_{(hkl)}$) can be estimated. The plots are illustrated in Figure 3 and the calculated ($D_{(hkl)}$) and ε values are presented in Table 1. The crystallite surface stress was calculated using the Uniform Stress Deformation Mode (USDM), which assumes linear proportionality between stress and strain, thus obeying Hooke's law:

$$Y = \frac{\sigma}{\varepsilon} \tag{3}$$

where Y is the modulus of elasticity or Young's modulus. Thus, substituting Eq 3 into 2 and rearranging gives Eq 4:

$$\beta_{(hkl)} \cos\theta = \frac{k\lambda}{D_{(hkl)}} + \frac{4\sigma \sin\theta}{Y_{(hkl)}} \tag{4}$$

In hexagonal crystallites like hydroxyapatite the elastic modulus $Y_{(hkl)}$ is dependent on crystallographic direction (normal to the set of (hkl) crystal lattice planes) and is expressed by Eq 5:

$$Y_{hkl} = \left(\frac{\left[h^2 + \frac{(h+2k)^2}{3} + \frac{(al)^2}{c} \right]^2}{S_{11}\left(h^2 + \frac{(h+2k)^2}{3} \right)^2 + S_{33}\left(\frac{al}{c} \right)^4 + (2S_{13} + S_{44})\left(h^2 + \frac{(h+2k)^2}{3} \left(\frac{al}{c} \right)^2 \right)} \right) \tag{5}$$

where the elastic compliances for the respective crystallographic directions are $S_{11} = 7.49 \times 10^{-12}$, $S_{33} = 10.9 \times 10^{-12}$, $S_{44} = 15.1 \times 10^{-12}$ and $S_{13} = -4.0 \times 10^{-12}$ $m^2 \cdot N^{-1}$ [18]. Thus, plotting 4 $\sin\theta/Y_{(hkl)}$ along the x-axis and $\beta_{(hkl)} \cos\theta$ along the y-axis produces a linear graph in which the slope (σ) and crystallite size ($D_{(hkl)}$) can be estimated. The plots are illustrated in Figure 3 and the calculated ($D_{(hkl)}$) and σ values are presented in Table 1. The anisotropic energy density (u) was estimated using the Uniform Deformation Energy Density Model (UDEDM), which modifies Eq 2 by substituting the strain energy for an elastic crystallite following Hooke's law, Eq 6 to produce Eq 7 below:

$$u = \frac{\varepsilon^2 Y_{(hkl)}}{2} \tag{6}$$

$$\beta_{(hkl)} \cos\theta = \frac{k\lambda}{D_{(hkl)}} + 4 \sin\theta \left(\frac{2u}{Y_{(hkl)}} \right)^{\frac{1}{2}} \tag{7}$$

Then plotting $\beta_{(hkl)}cos\theta$ along the y-axis and $4sin\theta(2u/Y_{(hkl)})^{1/2}$ along the x-axis, the anisotropic energy density u was estimated from the slope and the crystallite size was determined from the y-intercept. The plots are illustrated in Figure 3 and the calculated ($D_{(hkl)}$) and u values are presented in Table 1.

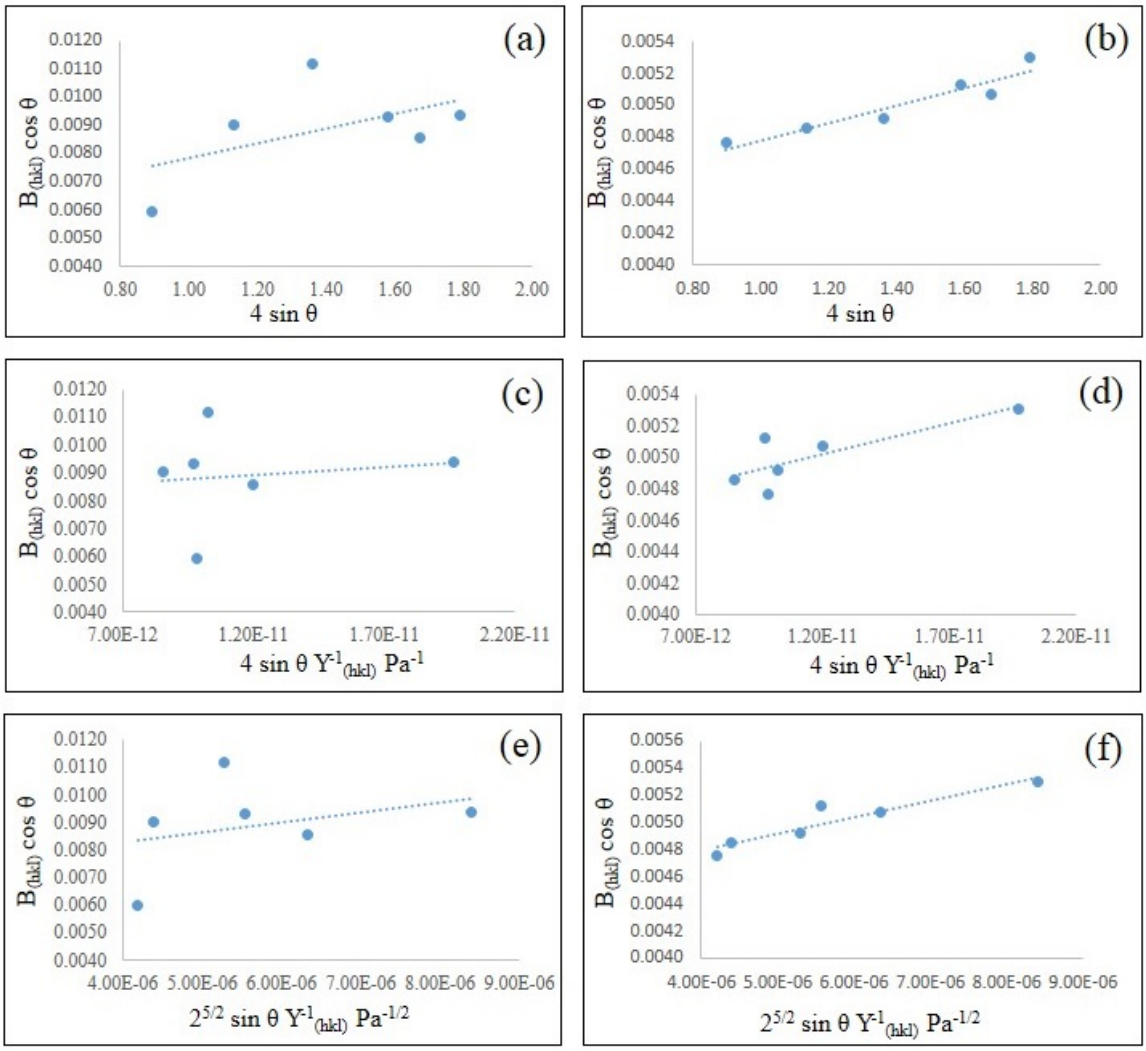

Figure 3. Plots of $\beta_{(hkl)}\cos\theta$ versus $4\sin\theta$; $\beta_{(hkl)}\cos\theta$ versus $4\sin\theta/Y_{(hkl)}$ and $\beta_{(hkl)}\cos\theta$ versus $4\sin\theta(2u/Y_{(hkl)})^{1/2}$ for as synthesized samples (a, c, e) and annealed (800 °C) samples (b, d, f).

Table 1. XRD peak analysis results of samples before and after annealing.

Sample	Scherrer(002) (nm)	UDM methods		USDM methods		UDEDM methods	
		$D_{(hkl)}$ (nm)	$\varepsilon \times 10^{-3}$	$D_{(hkl)}$ (nm)	σ (MPa)	$D_{(hkl)}$ (nm)	u (kJ/m^3)
As synthesized	23.28	26.35	2.586	16.81	55.28	20.28	19.03
Annealed at 800°C, 2h	29.11	32.75	0.549	30.43	38.65	32.1	10.99

Also calculated from the XRD data were the lattice constants (a, c) and the unit cell volume (V) of the respective samples using Eqs 8 and 9:

$$\frac{1}{d^2} = \frac{4}{3}\left(\frac{h^2 + hk + k^2}{a^2}\right) + \frac{l^2}{c^2} \tag{8}$$

$$V = \frac{\sqrt{3}\ a^2\ c}{2} = 0.866\ a^2 c \tag{9}$$

The calculated lattice constants and unit cell volumes obtained for the samples are presented in Table 2.

Table 2. Lattice parameters & unit cell volume of samples before and after annealing.

Sample	Lattice parameters		Unit cell volume
	a (Å)	c (Å)	V (Å^3)
As synthesized	9.4256	6.8933	530.351
Annealed at 800 °C for 2 h	9.4191	6.8988	530.042

Both Scherrer and Williamson–Hall analysis techniques revealed the product formed by annealing tended to have an increased crystallite size as seen in Table 1. The Williamson-Hall analysis also revealed the annealing process also reduced the strain in the crystalline structure. For instance, as seen in Table 1, the strain in the as-synthesized sample was 2.586×10^{-3}. But after annealing the sample strain was reduced to 0.549×10^{-3}. Similarly there was also a reduction in crystallite surface stress. As seen in Table 1, stress in the as-synthesized sample was 55.28 MPa and after annealing it was reduced to 38.65 MPa. There was also a corresponding reduction seen in energy densities. With the energy density reducing from 19.03 kJ/m^3 for the as-synthesized sample down to 10.99 kJ/m^3 for the annealed sample. Similar property changes resulting from annealing have also been reported in comparable studies by other researchers [19,20]. Also investigated were the lattice parameters and unit cell volumes of the samples. The results of the analysis is presented in Table 2 and reveals very little difference between the samples. A similar result was reported for a comparable study using similar annealing temperatures by Chaikina et al. [21].

3.2. Furher characterisations techniques

3.2.1. FTIR

FT-IR spectroscopy studies were carried out on all samples to confirm functional groups associated with the formation of the synthesized crystalline powders. Importantly, the studies revealed the absence of impurities in the samples. The studies also revealed a sharpening of the bands after annealing, which was an indication of increasing crystallinity, as seen in Figure 3. The as-synthesized spectra (a) in Figure 4 shows a number of characteristic bands normally associated with HAP. Moving from right to left, the bands occurring at 564 cm^{-1} and 601 cm^{-1} are the result of O–P–O vibrational modes. At 632 cm^{-1} a weaker hydroxyl vibrational mode was detected, while at 832 cm^{-1} there was a weaker band indicating the presence of carbonates. The next band was located at 961 cm^{-1} and indicates the symmetric stretching vibrations of the P-O mode. While the stronger bands located at 1032 cm^{-1} and 1092 cm^{-1} correspond to the $(PO_4)^{3-}$ functional group, and the weaker band located at 1384 cm^{-1} corresponds to the $(CO_3)^{2-}$ functional group. The smaller band located at 1644 cm^{-1} also corresponded to a $(CO_3)^{2-}$ functional group. The presence of carbonates in the samples is the result of interactions between the nano-HAP precursor alkaline solution and atmospheric carbon dioxide. This peak has been seen in several other comparable studies and

reported in the literature [22,23]. While the band located at 3432 cm^{-1} indicated the presence of absorbed water and the weaker band located at 3570 cm^{-1} corresponded to the vibrations of OH^- ions in the nano-HAP lattice. The slightly sharper bands in the annealed sample (b) indicates improved crystallinity of the nano-HAP and has been reported in the literature [24]. The absence of bands at 1644 and 1384 cm^{-1} is due to the loss of carbonate ions during heating in air and is typical when annealing temperatures are above 700 °C [25]. In addition, the loss of the broad band at 3432 cm^{-1} in the annealed sample is due to the loss of adsorbed water during the annealing process. In addition, EDS analysis of the samples was carried out during the manufacture of the nano-HAP and confirmed the elemental Ca/P ratio was maintained at 1.67 during synthesis. The analysis also confirmed the absence of impurities in the samples and the synthesis process produced high quality nano-HAP powders. Thus, confirming the results of the FT-IR spectroscopy studies. A representative EDS spectrum is presented in Figure 2b.

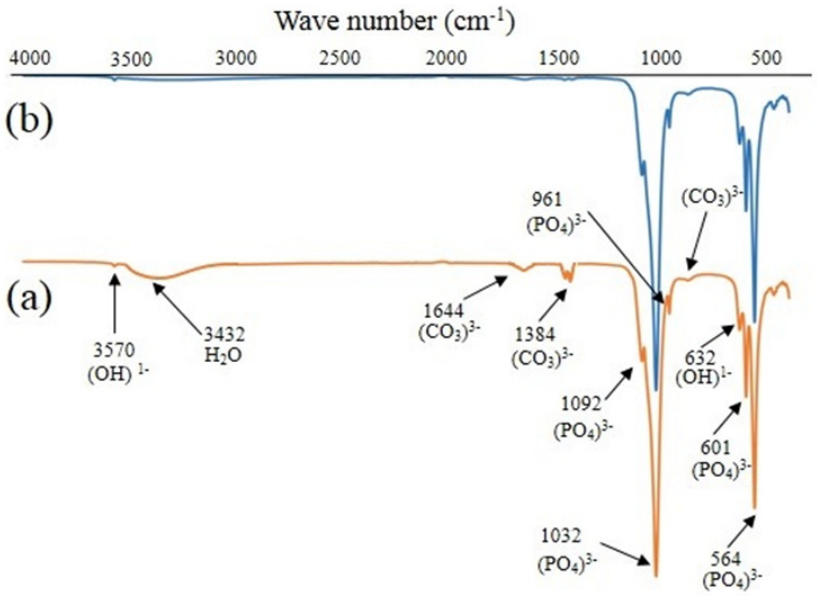

Figure 4. FTIR spectra: (a) as-synthesized nano-HAP and (b) nano-HAP annealed at 800 °C for 2 h.

3.2.2. Electron Microscopy confirmation

Moreover, to confirm the size and crystallinity of the HAP, electron microscopy was used. A high resolution TEM investigation was carried out on the as-synthesized nano-HAP powders and representative images are presented in Figure 4a,b. The nano-HAP particles were rod-like in shape with diameters ranging from 18 nm up to 30 nm, and lengths ranging from 130 nm to around 200 nm. The average aspect ratio of the particles was found to be typical around 1:7. The particles tended to cluster to form large agglomerations as seen in Figure 5b. The SAED pattern (Figure 5a) also corresponded to the crystal planes as observed by XRD analysis. The rings on the SAED pattern belonged to (200), (111), (002), (102), (210), (112), (300), (202), (301), (130,310) and (222) crystal planes with d-spacing of 0.404 nm, 0.385 nm, 0.349 nm, 0.329 nm, 0.308 nm, 0.278 nm, 0.270 nm, 0.260 nm, 0.254 nm, 0.227 nm and 0.191 nm, respectively. It should be noted that the crystal planes observed through SAED analysis were in comparison to the planes observed by X-ray powder

diffraction. Similar as-synthesized nanoparticle sizes were also seen in FESEM images, as seen in Figure 5c.

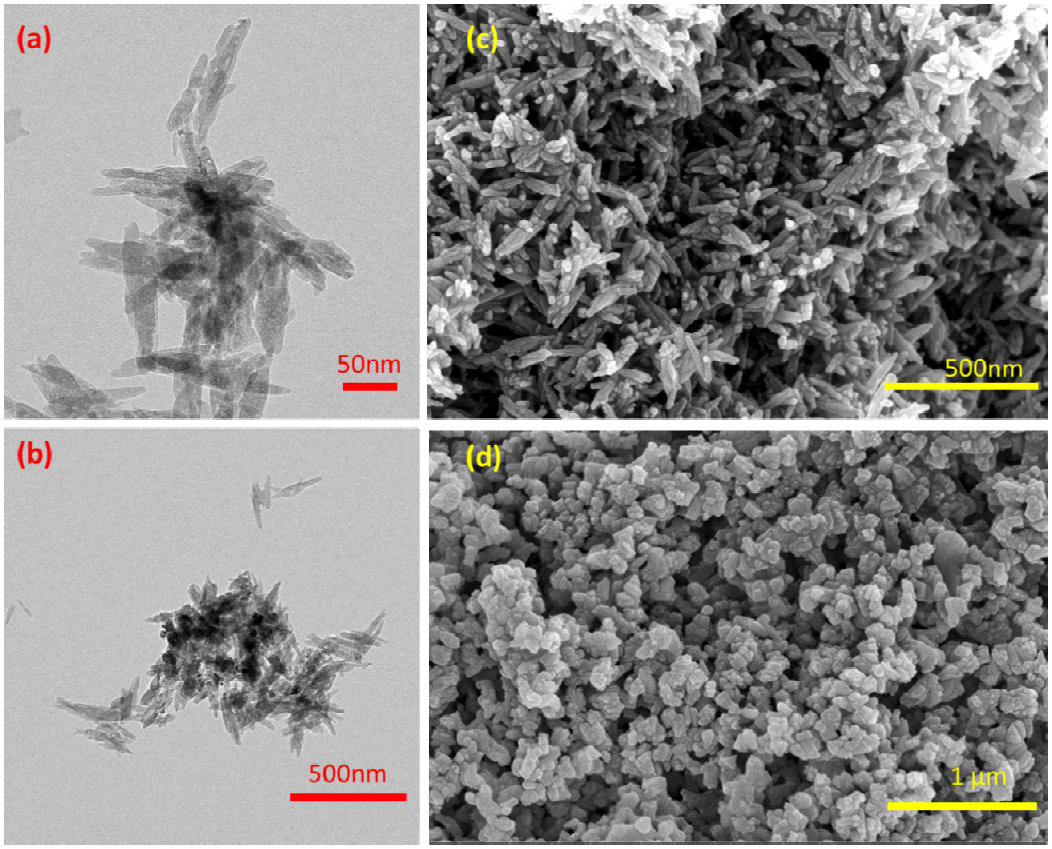

Figure 5. (a) Transmission Electron Micrographs of as-synthesized nano-HAP particles; (b) clustering of as-synthesized particles; (c) representative FESEM image of highly agglomerated as synthesized nano-HAP, and (d) SEM showing the physical effect on HAP sample as a result of annealing at 800 °C.

Figure 5c also confirms the tendency of the nanoparticles to cluster and form dense agglomerations. Figure 5d presents a representative FESEM image of an annealed (800 °C) sample. Inspection of the image reveals a different particle size range and morphology compared to the non-annealed samples. The annealed nanoparticles have a granular and a rough irregular rectangular morphology, with sizes ranging from 70 to 150 nm. Importantly, the present study has demonstrated the combined ultrasonic and microwave based synthesis procedure is capable of producing two different morphological types. Purely ultrasonic synthesis methods generally produce spherical morphologies. But the present study has shown the additional microwave irradiation step promotes an orientated crystal growth to produce rod-like shaped nano-HAP particles. Furthermore, subsequent annealing of powder samples at 800 °C also generated morphological changes in the nanoparticles. However, lower annealing temperatures of around 400 °C (images not shown) did not show any morphological changes in the powders. In order to understand the morphological approach of using synthesized nano-hap powders as a potential dental restorative system, the micrographs of synthesized hydroxyapatite crystals were compared to the scanning electron micrographs of

extracted human wisdom tooth (shown in Figure 6). The representative images show a cross section of chipped tooth enamel detailing the fine needle shaped micro-structures and architecture.

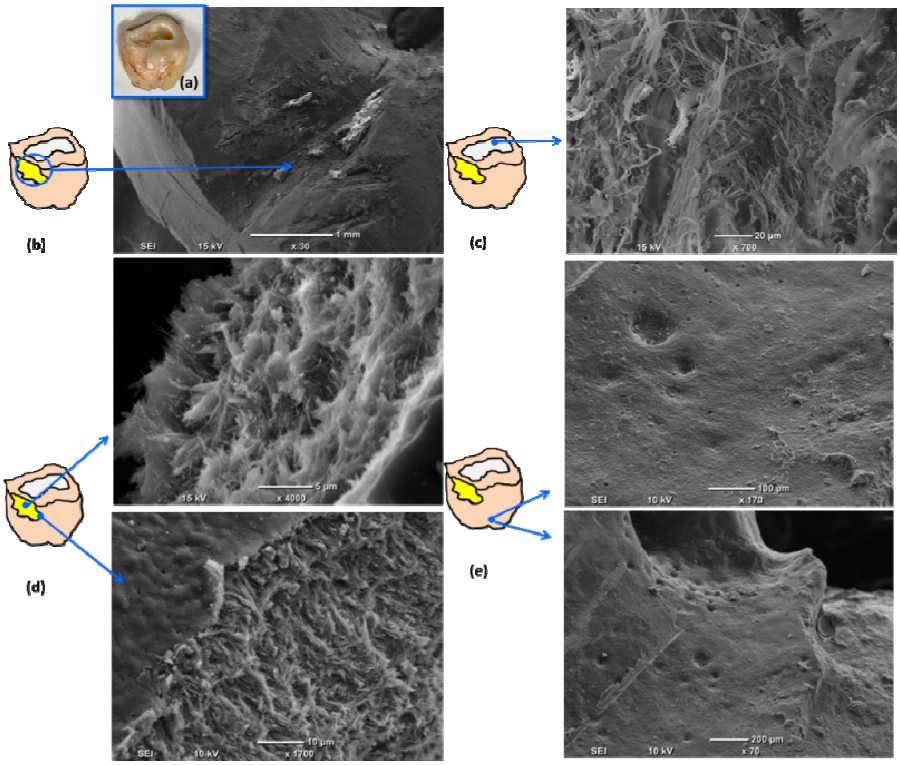

Figure 6. (a) Optical image of extracted human wisdom tooth, (b) Schematic representation of area chipped on tooth and respective scanning electron image of area highlighted, (c), (d) and (e) are scanning electron micrographs of highlighted areas as shown in respective schematic diagrams.

4. Conclusion

Highly crystalline pure nano-HAP powders were successfully synthesized using a combined ultrasonic and microwave heating based method. During the ultrasonic synthesis stage, the reaction mixture pH was stabilized at 9 and the Ca/P ratio of 1.67 was maintained. After the microwave heating treatment, the nano-HAP powders were found to be highly crystalline in nature and were rod-like in shape. The average aspect ratio of the particles was found to be around 1:7, with diameters ranging from 18 nm up to 30 nm. Annealing for 2 h at 800 °C transformed the nanoparticle morphology to a rough irregular rectangular and granular nature, with sizes ranging from 70 to 150 nm. There was good agreement between the crystallite size values estimated by Williamson–Hall analysis methods like (UDM), (USDM) and (UDEDM). With the annealed sample showing the closest agreement between crystallite size for the respective models. The calculated crystallite size of all models tended to be larger than those predicted by the Scherrer method. The present study also found instrumental effects and lattice strain in the samples can significantly contribute to X-ray peak broadening. Thus, in the case of nanomaterials, both instrumental and lattice strain broadening must be taken into account when calculating microstructural parameters like crystallite size, lattice strain,

stress and energy density. The study has also demonstrated that nano-HAP powders with crystallite sizes and morphologies similar to those found in dental hard tissues can be synthesized using the combined ultrasonic and microwave heating-based method presented in this article.

Acknowledgments

Supriya Rattan would like to acknowledge Murdoch University for providing her PhD Scholarship. The authors would also like to thank Centre for Microscopy, Characterisation and Analysis, University of Western Australia for TEM and SEM imaging.

Conflict of interest

The authors declare that there is no conflict of interests

References

1. Kerebel B, Daculsi G, Kerebel LM (1979) Ultrastructural studies of enamel crystallites. *Dent Res* 58: 844–851.
2. Imbeni V, Kruzic JJ, Marshall GW, et al. (2005) The dentin-enamel junction and the fracture of human teeth. *Nature Mater* 4: 229–232.
3. Kalita SJ, Bhardwaj A, Bhatt HA (2007) Nanocrystalline calcium phosphate ceramics in biomedical engineering. *Mater Sci Eng C-Mater* 27: 441–449.
4. Cai Y, Tang R (2008) Calcium phosphate nanoparticles in biomineralization and biomaterials. *J Mater Chem* 18: 3775–3787.
5. Blom A (2007) Which scaffold for which application? *Curr Orthopaed* 21: 280–287.
6. Habibovic P, de Groot K (2007) Osteoinductive biomaterials—properties and relevance in bone repair. *J Tissue Eng Regen M* 1: 25–32.
7. Li L, Pan H, Tao J, et al. (2008) Repair of enamel by usinghydroxyapatite nanoparticles as the building blocks. *J Mater Chem* 18: 4079–4084.
8. Tschoppe P, Zandim D, Martus P, et al. (2011) Enamel and dentine remineralization by nano-hydroxyapatite toothpastes. *J Dent* 39: 430–437.
9. Meffert RM, Thomas JR, Hamilton KM, et al. (1985) Hydroxylapatite as an alloplastic graft in the treatment of human periodontal osseous defects. *J Periodontol* 56: 63–73.
10. Piecuch JF (1986) Augmentation of the atrophic edentulous ridge with porous replamine form hydroxyapatite (Interpore-200). *Dent Clin North Am* 30: 291–305.
11. Jean A, Kerebel B, Kerebel LM, et al. (1988) Effects of various calcium phosphate biomaterials on reparative dentin bridge formation. *J Endodont* 14: 83–87.
12. Pissiotis E, Spangberg LS (1990) Biological evaluation of collagen gels containing calcium hydroxide and hydroxyapatite. *J Endodont* 16: 468–473.
13. Rigo EC, Boschi AO, Yoshimoto M, et al. (2004) Evaluation *in vitro* and *in vivo* of biomimetic hydroxyapatite coated on titanium dental implants. *Mater Sci Eng C-Mater* 24: 647–651.
14. Okada M, Furuzono T (2012) Hydroxylapatite nanoparticles: Fabrication methods and medical applications. *Sci Technol Adv Mater* 13: 064103.

15. Zhou H, Lee J (2011) Nanoscale hydroxyapatite particles for bone tissue engineering. *Acta Biomater* 7: 2769–2781.
16. Prabhu YT, Rao KV, Kumar VSS, et al. (2014) X-ray analysis by Williamson–Hall and size-strain plot methods of ZnO nanoparticles with fuel variation. *WJNSE* 4: 43743.
17. Venkateswarlu K, Bose AC, Rameshbabu N (2010) X-ray peak broadening studies of nanocrystalline hydroxyapatite by Williamson–Hall analysis. *Physica B* 405: 4256–4261.
18. Gray DE (1972) *American Institute of Physics Handbook*, New York: McGraw-Hill Book Company.
19. Venkateswarlu K, Sreekanth D, Sandhyarani M, et al. (2012) X-ray peak profile analysis of nanostructured hydroxyapatite and fluorapatite. *Int J Biosci Biochem Bioinform* 2: 389–393.
20. Liangzhi G, Weibin Z, Yuhui S (2016) Magnesium substituted hydroxyapatite whiskers: synthesis, characterization and bioactivity evaluation. *RSC Adv* 6: 114707–114707.
21. Chaikina MV, Bulina NV, Prosanov IYU, et al. (2012) Mechanochemical synthesis of hydroxyapatite with SiO_4 substitutions. *Chem Sustain Dev* 20: 431–443.
22. Wang YJ, Chen JD, Wei K, et al. (2006) Surfactant-assisted synthesis of hydroxyapatite particles. *Mater Lett* 60: 3227–3231.
23. Beckett EL, Lawrence NS, Tsai YC, et al. (2001) Bioanalytical utility of sonovoltammetry. *J Pharmaceut Biomed* 26: 995–1001.
24. Panda RN, Hsieh MF, Chung RJ, et al. (2003) FTIR, XRD, SEM and solid state NMR investigations of carbonate-containing hydroxyapatite nano-particles synthesised byhydroxide-gel technique. *J Phys Chem Solids* 64: 193–199.
25. Kannan S, Rocha JHG, Ventura JMG, et al. (2005) Effect of Ca/P ratio of precursors on the formation of different calcium apatite ceramics—an X-ray diffraction study. *Scripta Mater* 53: 1259–1262.

AIMS Press